INTENSITY-RESOLVED ABOVE THRESHOLD IONIZATION YIELDS OF ATOMS WITH ULTRASHORT LASER PULSES

A Thesis

by

NATHAN ANDREW HART

Submitted to the Office of Graduate Studies of
Texas A&M University
in partial fulfillment of the requirements for the degree of

MASTER OF SCIENCE

August 2011

Major Subject: Physics

Intensity-resolved Above Threshold Ionization Yields of Atoms with Ultrashort Laser Pulses

INTENSITY-RESOLVED ABOVE THRESHOLD IONIZATION YIELDS OF ATOMS WITH ULTRASHORT LASER PULSES

A Thesis

by

NATHAN ANDREW HART

Submitted to the Office of Graduate Studies of
Texas A&M University
in partial fulfillment of the requirements for the degree of

MASTER OF SCIENCE

Approved by:

Co-Chairs of Committee,	Gerhard Paulus
	Alexandre Kolomenski
Committee Members,	Hans Schuessler
	Winfried Teizer
	Stephen Fulling
Head of Department,	Edward Fry

August 2011

Major Subject: Physics

ABSTRACT

Intensity-resolved Above Threshold Ionization Yields of Atoms with Ultrashort Laser Pulses.

(August 2011)

Nathan Andrew Hart, B.S., Texas A&M University

Co-Chairs of Advisory Committee: Dr. Gerhard Paulus
Dr. Alexandre Kolomenski

The above threshold ionization (ATI) spectra provide a diversity of information about a laser-atom ionization process such as laser intensity, pulse duration, carrier envelope phase, and atomic energy level spacing. However, the spatial distribution of intensities inherent in all laser beams reduces the resolution of this information. This research focuses on recovering the intensity-resolved ATI spectra from experimental data using a deconvolution algorithm.

Electron ionization yields of xenon were measured for a set of laser pulse intensities using a time of flight (TOF) setup. Horizontally polarized, unchirped, 50fs pulses were used in the ionization process. All laser parameters other than the radiation intensity were held constant over the set of intensity measurements. A deconvolution algorithm was developed based on the experimental parameters. Then the deconvolution algorithm was applied to the experimental data to obtain the intensity-resolved total yield probability and ATI spectra. Finally, an error analysis was performed to determine the stability and accuracy of the algorithm as well as the quality of the data.

It was found that the algorithm produced greater contrast for peaks in the ATI spectra where atom specific resonant behavior is observed. Additionally, the total yield probability showed that double ionization may be observed in the ionization yield. The error analysis revealed that the algorithm was stable under the experimental conditions for a range of intensities.

DEDICATION

To my Lord and Savior Jesus Christ.

ACKNOWLEDGEMENTS

I would like to thank my advisor, Dr. Gerhard Paulus, and Dr. Hans Schuessler for their advice and for making this research possible. Additionally, I would like to thank the co-chair of my committee, Dr. Alexandre Kolomenski, for his guidance concerning my research and the completion of this thesis. To the committee members, Dr. Stephen Fulling and Dr. Winfreid Tiezer, I am grateful for all their time and help. I would like to thank Dr. James Strohaber for detailed discussions and assistance related to this experiment.

I acknowledge the Department of Physics at Texas A&M and the US Air Force for their financial support over the past few years.

It has been a privilege to work in the Attosecond and Fewcycle Laser Laboratory with Fransisco Pham, Feng Zhu, Ricardo Nava, Necati Kaya, Gamze Kaya and Cade Perkins.

I would like to thank my ReJOYce IN JESUS family for their prayers. And finally, a special thanks goes to my mother, father and sister for their encouragement and support.

TABLE OF CONTENTS

Page

ABSTRACT iii

DEDICATION v

ACKNOWLEDGEMENTS vi

TABLE OF CONTENTS vii

LIST OF FIGURES ix

1. INTRODUCTION AND LITERATURE REVIEW 1

2. IONIZATION OF ATOMS 3

    A. Ponderomotive Energy 3
    B. Multiphoton Ionization 7
    C. Tunneling Ionization 9
    D. Over the Barrier Ionization 10
    E. Above Threshold Ionization 12

3. SCHEME FOR REALIZATION OF INTENSITY-RESOLVED IONIZATION RATES 15

    A. Basic Principle 15
    B. Experimental Setup 15
    C. Experimental Equipment 17

4. CONVERTING FROM TOF TO ENERGY SPECTRA 20

    A. The Format of Recorded Data 20
    B. Discrete Conversion to Energy Spectra 22
    C. Continuous Conversion to Energy Spectra 22

5. GAUSSIAN BEAM GEOMETRY 24

6. REMOVING INTENSITY INTEGRATION 26

    A. Intensity Difference Scanning 26
    B. Analytical Volume Deconvolution in M Dimensions 30
    C. Implementation of the Volume Deconvolution 32
    D. Error Propagation Through the Algorithm 33
    E. Runge's Phenomenon 35

7. ANALYSIS OF EXPERIMENTAL DATA 37

Page

8. SUMMARY AND CONCLUSION 42

REFERENCES 43

VITA 45

LIST OF FIGURES

Page

Fig. 1. Electrons being pushed away from the center of the focus. 4

Fig. 2. Ionization in a low intensity field. 6

Fig. 3. Photon absorption and spontaneous reemission.. 7

Fig. 4. Photoionization due to the photoelectric effect (A) and multi-photon absorption (B).....8

Fig. 5. Tunneling Ionization.....9

Fig. 6. A graphical depiction of over the barrier ionization. 11

Fig. 7. A graphical depiction of the ATI process. Here the electron absorbs an integer number of photons whose total energy exceeds V_{IE} by more than one photon.....13

Fig. 8. Channel closing for the E_1 and E_2 peaks of a simulated ATI spectrum. 14

Fig. 9. The experimental setup. 16

Fig. 10. A photograph taken of the ATI apparatus and related components.....17

Fig. 11. The essential components of the ATI apparatus. 18

Fig. 12. A visual representation of the time bins $t_{b,i}$ and their electron counts $S_{t,i}$.....21

Fig. 13. A depiction of the three-dimensional iso-intensity shells. 25

Fig. 14. An example schematic in one dimension showing how volume elements are related to peak intensities.. 27

Fig. 15. A scheme showing the relationship between the volume elements ($V_{1,1}$, $V_{1,2}$, $V_{2,2}$) and their respective probabilities ($P(I_1)$, $P(I_2)$, $P(I_2)$).....28

Fig. 16. Graphical depiction of the IDS algorithm using two intensities. 29

Fig. 17. V and V^{-1} portrayed as $N \times N$ matrix transformations between $\boldsymbol{Y}$ and $\boldsymbol{P}$. 30

Fig. 18. Interpolating polynomials of degree 5 (blue) and 9 (green) and their

Page

generation function (red) 35

Fig. 19. The photoelectron yield rate for xenon 37

Fig. 20. The Runge divergence calculated for the model xenon probability function P(I) using (6.26) 38

Fig. 21. The intensity-resolved probability of the data 39

Fig. 22. Intensity-resolved ATI energy spectra at 7.8×10^{13} W/cm^2. 40

Fig. 23. Intensity-resolved ATI energy spectra at 7.2×10^{13} W/cm^2. 41

1. INTRODUCTION AND LITERATURE REVIEW

When performing experiments to study the atomic and/or molecular interaction with a laser field the detection information often comes from ionized electron or fluorescence photon signals. The signal probability is a function of the radiation intensity and wavelength where the atom or molecule is located.

The focal volume of a laser contains a continuum of intensities that vary both radially and longitudinally with respect to the axis of propagation and range from zero to some peak intensity. Each intensity contributes a unique ion yield rate depending on the probability of ionization and the volume of that radiation intensity. It has been demonstrated that the position of an ion within the focus can be measured to high precision ($\sim 1\mu m$) (Strohaber, 2008). However, measuring devices are rarely able to determine the location within the focus that an electron originated from. For instance, to distinguish two coaxial electrons in an electric field-free region with $1.5eV$ of kinetic energy and a separation distance of $10\mu m$ would require data acquisition electronics with $13ps$ resolution. For photons of the same energy and spatial separation it would require $30fs$ temporal resolution. Typical fast data acquisition electronics have temporal resolutions of a few hundred picoseconds. The insufficient temporal resolution results in integration of the signal over the entire focal volume of the laser.

This thesis follows the style of *Advances in Atomic, Molecular and Optical Physics*.

Several methods have been employed to work around this difficulty. Hansch and Van Woerkom (1996) used a two dimensional z-axis measurement to obtain a photoelectron spectra with less intensity integration than a typical three-dimensional focal volume experiment. They noted that if a thin cross-section of a laser focus Δz is taken, the ratios of volumes occupied by different intensities changes as a function of the longitudinal variable z. By choosing a z position where the desired intensity spatially dominates, one can obtain a more selective intensity measurement. Walker *et al.* (1998) added an algorithm to the above z selection method to remove all radial volume integration while maintaining the small integration from the thickness of the slice Δz. To do this they analytically deconvolved the volume integration in two dimensions (radial and azimuthal) to obtain the probability of ionization as a function of intensity. Bryan *et. al*. (2006a) improved upon this algorithm, now termed Intensity Selective Scanning (ISS), by accounting for laser diffraction effects in the focal volume. Bryan *et. al.* (2006b) used this improved ISS algorithm to investigate intensity resolved ionization rates of higher charged states. While they were able to find the total ionization rate for a specific intensity, they did not obtain an intensity-resolved electron spectra.

The aim of this thesis is to demonstrate a deconvolution algorithm that can be used to obtain intensity-resolved photoelectron spectra. This would allow us to observe the appearance of Rabi oscillations and AC Stark shifts within the atomic energy levels.

2. IONIZATION OF ATOMS

A. Ponderomotive Energy

A free (continuum) electron in an oscillating electric field, $\boldsymbol{\mathcal{E}}(t) = \mathcal{E}_0 \sin \omega t \, \hat{\boldsymbol{x}}$, absorbs kinetic energy and oscillates slightly out of phase with the field. The free electron however retains the frequency of the oscillating field since this field is the only applied force. This can be seen by defining the Lagrangian for linearly polarized continuous wave radiation:

$$L = \frac{1}{2} m_e \dot{\boldsymbol{x}}^2 - e\boldsymbol{\mathcal{E}} \cdot \boldsymbol{x} \tag{2.1}$$

Plugging equation (2.1) into Lagrange's equation of motion and integrating successively with respect to time gives the velocity and position of the "classical" electron:

$$x(t) = \frac{e\mathcal{E}_0}{\omega^2 m_e} \sin \omega t + v_d t + x_0 \tag{2.2}$$

$$\dot{x}(t) = \frac{e\mathcal{E}_0}{\omega m_e} \cos \omega t + v_d \tag{2.3}$$

where v_d is the drift velocity and x_0 is the initial position of the electron when it was ionized. Using the definitions $I_0 \equiv c\epsilon_0 \mathcal{E}_0^2/2$ and $\omega = 2\pi c/\lambda$ and neglecting the drift velocity, the time averaged kinetic energy or ponderomotive energy in electron volts (eV) of such an electron is:

$$U_P = \frac{1}{2} m_e \langle \dot{x}^2 \rangle \tag{2.4}$$

$$= \frac{e^2 \mathcal{E}_0^2}{4 m_e \omega^2} \tag{2.5}$$

$$= 9.33 \times 10^{-14} I_0[\mathrm{W/cm^2}]\lambda^2[\mu\mathrm{m^2}] \tag{2.6}$$

This quantity is important because an electron in a finite laser beam of sufficiently long pulse duration will on average gain this energy, $\widetilde{U}_P$, in the form of translational kinetic energy. Since for a Gaussian beam the local electric field amplitude as a function of the radius in cylindrical coordinates is:

$$\mathcal{E}(r, z = 0) = \mathcal{E}_0\, e^{-r^2/w_0^2} \tag{2.7}$$

replacing $\mathcal{E}_0$ with $\mathcal{E}(r, 0)$ gives the local ponderomotive energy:

$$\widetilde{U}_P(r) = U_P e^{-2r^2/w_0^2} \tag{2.8}$$

where the azimuthal dependence has been neglected. This ponderomotive energy acts as an electric potential and provides a radial force $\boldsymbol{R}_P(r)$ to the electron due to the spatial variation in the field (see Fig. 1).

$$\boldsymbol{R}_P(r) = -\boldsymbol{\nabla}_{\boldsymbol{r}}\widetilde{U}_P(r) \tag{2.9}$$

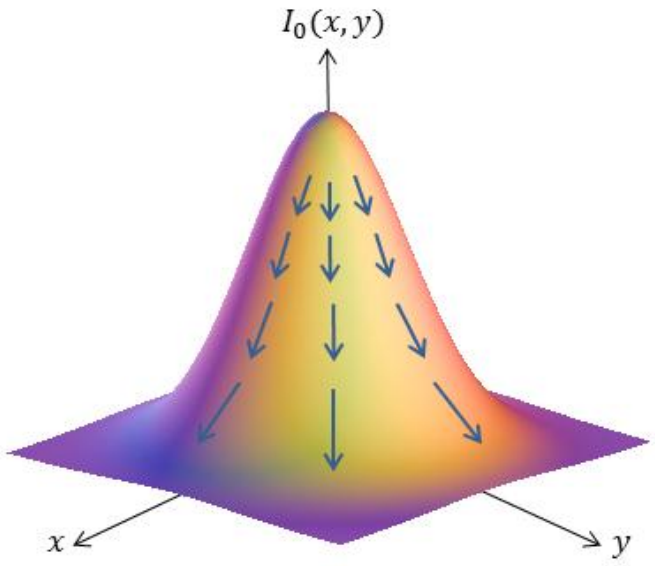

Fig. 1. Electrons being pushed away from the center of the focus.

If the electron is initially at a radius r_0 prior to being accelerated, then the work done on the electron as it is pushed out of the field is:

$$W_P = -\int_{r_0}^{\infty} \boldsymbol{R}_P(r) \cdot d\boldsymbol{r} \tag{2.10}$$

$$= \widetilde{U}_P(r_0) \tag{2.11}$$

This means that the electron will gain a translational kinetic energy equal to the ponderomotive energy where it initially experienced the field. In calculating W_P, the upper bound of the integral implies that the radiation is continuous wave (CW). However, for sufficiently short pulses the electron may not have enough time to be displaced out of the field and, as a result, not gain the full $\widetilde{U}_P(r_0)$. A rough estimate of the necessary laser parameters for equation (2.11) to hold can be obtained by equating the kinetic energy of the free electron to $U_P/2$ and finding the distance it travels for pulse duration τ_d. For example, a pulse of wavelength $\lambda = 800\text{nm}$, duration $\tau_d = 100\text{fs}$ and peak intensity $I_0 = 10^{13}\text{W/cm}^2$ would move an electron less than 50nm away from the center of the beam. This is negligible compared to a typical beam waist of $w_0 \sim 10\mu\text{m}$, and as a result the upper bound of the integral (2.10) is approximately r_0.

When an electric field is applied to an atom, the energy levels change by a value known as the Stark shift. Through a lengthy quantum mechanical calculation (Delone & Krainov, 1994) it is found that the dynamic or AC Stark shift of an atomic energy level $E_i \ll \hbar\omega$ due to an oscillator field is approximated by:

$$\delta E_i \approx \frac{e^2 \mathcal{E}(r_0)^2}{4 m_e \omega^2} \tag{2.12}$$

$$= U_P(r_0) \tag{2.13}$$

It is remarkable that the AC Stark shift under the above restriction is equal to the ponderomotive energy $U_P(r_0)$ provided by the field. One consequence of this is that the highest "continuum" state $E_i \approx 0$, is increased in the following manner: $E_i \rightarrow E_i + \delta E_i$. To be ionized the electron must now gain an energy:

$$E > U_P(r_0) + V_{IE} \tag{2.14}$$

where V_{IE} is the ionization energy of the unperturbed atom (see Fig. 2).

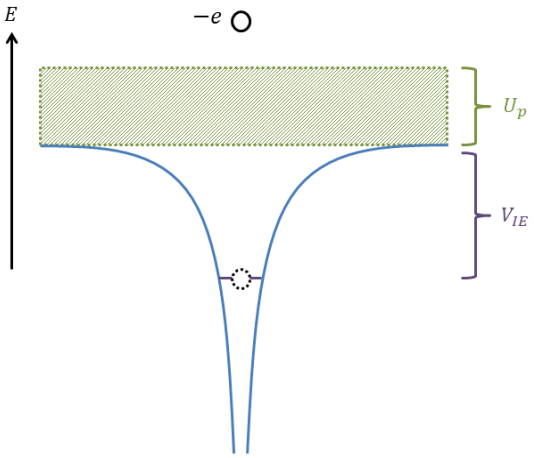

Fig. 2. Ionization in a low intensity field.

Once ionized the electron is pushed along the radiation energy gradient towards lower ponderomotive energies. For sufficiently long laser pulse durations ($\tau_d \gg 1\text{ps}$) and large intensities ($I_0 > 10^{13}\text{W/cm}^2$) at $\lambda = 800\text{nm}$ the electron will regain the kinetic energy $U_P(r_0)$ lost through the AC Stark shift as it travels away from the atom. However, for short laser pulses ($\tau_d < 50\text{fs}$) even intensities as high as $I_0 \sim 10^{15}\text{W/cm}^2$ will not be sufficient to recover the lost energy.

B. Multiphoton Ionization

There are three general ways in which photoionization can be described. For the lowest intensities, a process analogous to the photoelectric effect occurs. In the photoelectric effect, an atom is ionized when a bound electron absorbs a photon whose energy $\hbar\omega$ exceeds the atomic potential energy V_{IE}. The photoelectric effect follows the rule of being independent of the radiation intensity because the decay rate of the excited atom is much faster than the absorption rate of new photons. Thus, for a wide range of intensities (in Xenon: $I_0 < 10^{11}\mathrm{W/cm^2}$), photons with energy $\hbar\omega \ll V_{IE}$ are reemitted by the atom (see Fig. 3).

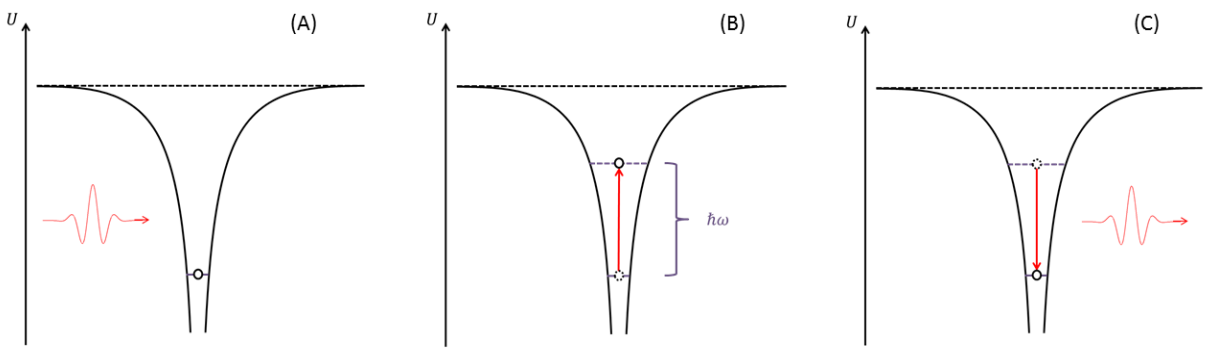

Fig. 3. Photon absorption and spontaneous reemission. The photon in red and the unexcited atom (A). The excited atom (B). Spontaneous emission of a photon (C).

However, increasing the radiation intensity I_0 above a certain threshold, called the appearance intensity I_{ap}, allows the photon absorption rate to exceed the decay rate. It is then possible to ionize the atom through an absorption of several photons as the sum of the photon energies exceeds the ionization potential.

$$\sum_i \hbar\omega_i > V_{IE} \tag{2.15}$$

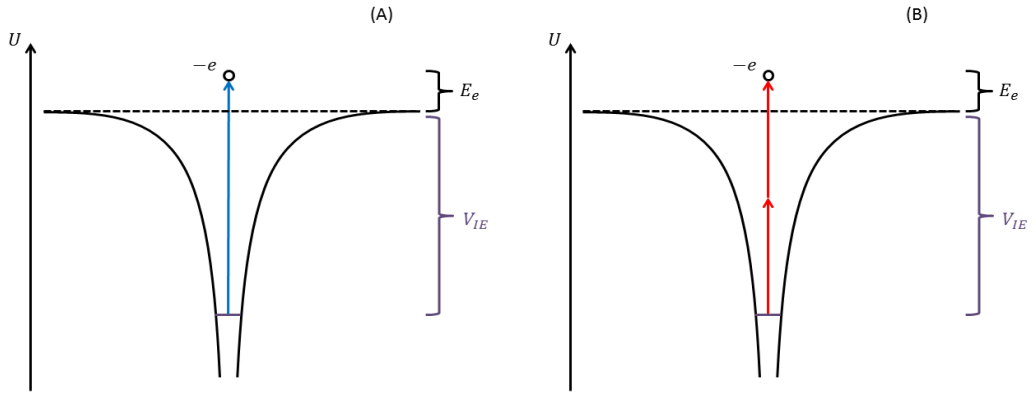

Fig. 4. Photoionization due to the photoelectric effect (A) and multi-photon absorption (B).

This process is referred to as multi-photon ionization (MPI), and can be viewed as a generalization of the photoelectric effect (see Fig. 4). For a broadband laser the electron can absorb several photons each with a unique energy present in the spectrum. But for simplicity, equation (2.16) depicts the interaction of monochromatic radiation with the atom "A":

$$n\hbar\omega + A \rightarrow e^- + A^+ \tag{2.16}$$

where n is the number of photons absorbed, $\hbar\omega$ is the energy of each photon, e^- is the ejected electron, A is the prepared target, and A^+ is the final state of the target. The energy of the electron is then:

$$KE = n\hbar\omega - V_{IE} \tag{2.17}$$

where V_{IE} is the potential energy of the electron for atom A. The radiation field is viewed as perturbation to the atomic potential well and perturbation theory can be used to find the ionization probability $P(I)$. $P(I)$ is proportional to the radiation intensity I to the power equal to the order of the multi-photon ionization:

$$P(I) \propto I^m \tag{2.18}$$

where m satisfies $1 \geq m - \frac{V_{IE}}{\hbar\omega} \geq 0$.

C. Tunneling Ionization

As an atom interacts with an oscillating electric field, the Coulomb potential of the initially unperturbed atom begins to sway back and forth in phase with the field. This is related to the variations of the effective potential of the atom:

$$V(x) = -\frac{1}{4\pi\epsilon_0}\frac{e^2 Z}{x} - e\boldsymbol{\mathcal{E}}_0(t)\cdot\boldsymbol{x} \tag{2.19}$$

$$= -\frac{1}{4\pi\epsilon_0}\frac{e^2 Z}{x} - e(\boldsymbol{\mathcal{E}}_0 \sin[\omega t])\cdot\boldsymbol{x} \tag{2.20}$$

where Z is the charge state of the atom, $\boldsymbol{x}$ is the distance away from the nucleus, $\mathcal{E}_0$ is the radiation field amplitude, ω is the frequency of the oscillation and t is the time variable. For sufficiently large electric fields, this effective potential of the atom will "dip" down, creating a well that the bound electron can tunnel out of (see Fig. 5). This is referred to as tunneling ionization (TI).

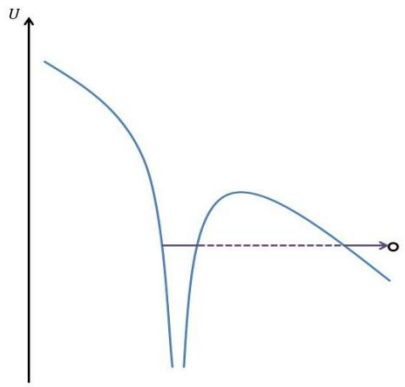

Fig. 5. Tunneling Ionization. The electron tunnels (dashed line) out of the atom and into the continuum.

The average tunneling time τ is determined by the potential barrier height and thickness. The Keldysh tunneling parameter γ is a metric for determining when the intensity is high enough to describe the ionization mainly through a tunneling process. The parameter γ has two equivalent representations (Keldysh, 1965):

$$\gamma = \frac{\omega\tau}{2\pi} \tag{2.21}$$

$$= \left(\frac{V_{IE}}{2U_P}\right)^{\frac{1}{2}} \tag{2.22}$$

where ω is the frequency of the oscillating electric field, V_{IE} is the ionization potential and $U_P$is the ponderomotive potential. The first representation gives an intuitive picture of the tunneling process. If the period of the laser, $2\pi/\omega$, is comparable to the tunneling time, τ, then tunneling becomes probable. Hence $\gamma \simeq 1$ is a necessary but not sufficient condition to imply electron tunneling out of the atom. The second representation is more useful for experimental research because it can be easily calculated. V_{IE} is usually found in published atomic and molecular reference materials and U_P can be calculated from equation (2.6). The utility of the Keldysh parameter itself comes from its ability to distinguish between MPI ($\gamma \gg 1$) and TI ($\gamma \simeq 1$). However, when γ approaches unity a mixture of the two processes maybe seen in experiment because both MPI and TI become probable to occur.

D. Over the Barrier Ionization

If the laser intensity is large enough, the Coulomb potential may no longer be higher than the unperturbed ground state. In this case, there is no longer a bound state for

the outer most electron. This electron is then said to be freed through Over The Barrier Ionization (OTBI).

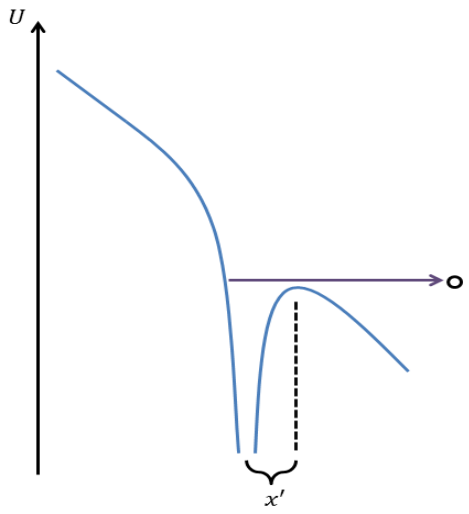

Fig. 6. A graphical depiction of over the barrier ionization.

To gain a qualitative understanding of the process we ignore any longitudinal electric field components of the uncollimated beam and reduce equation (2.19) to one dimension. This paraxial approximation is only valid where the beam makes a negligible angle with the axis of propagation. The minimum electric field required to induce OTBI can then be found by first noting that the condition for OTBI is the following:

$$-V_{IE} > -\frac{1}{4\pi\epsilon_0}\frac{e^2 Z}{|x'|} - e\mathcal{E}_0 x' \tag{2.23}$$

This means that the ground state energy of the unperturbed atom is greater than the peak potential energy of the atom in the radiation field (see Fig. 6). We can find x' from the equation $dV(x = x')/dx = 0$. This gives:

$$x' = \sqrt{eZ/4\pi\epsilon_0\mathcal{E}_0} \tag{2.24}$$

for the distance away from the nucleus where the potential starts to dip back down. Plugging equation (2.24) into equation (2.23) gives:

$$\mathcal{E}_0 > \frac{\pi \epsilon_0 {V_{IE}}^2}{e^3 Z} \tag{2.25}$$

$$I_0 > c\epsilon_0^3 \frac{\pi^2 {V_{IE}}^4}{2\, e^6 Z^2} \tag{2.26}$$

Note that while MPI and TI are functions of two laser parameters I_0 and λ, OTBI is only a function of I_0. This is because of the relatively small mass, and thus inertia, of the electron. An unbound electron with one unit of photon energy $\hbar\omega < 5\text{eV}$ will, in half a laser cycle, travel a distance more than 10 times the Bohr radius a_0. For comparison the neutral xenon atom is approximately twice the Bohr radius. This means that for a wide range of photon energies the wavelength dependence is negligible.

E. Above Threshold Ionization

During irradiation, electrons in the target atom or molecule may absorb more photons than are needed to exceed the ionization threshold V_{IE}. The absorption of additional photon energy above the minimum ionization threshold is referred to as Above Threshold Ionization (ATI) (see Fig. 7). This is expressed mathematically by:

$$E_e > \hbar\omega \tag{2.27}$$

where E_e is the kinetic energy of the electron in the continuum due to photon absorption. ATI may, and typically does occur in all three of the above mentioned ionization mechanisms (MPI, TI and OTBI).

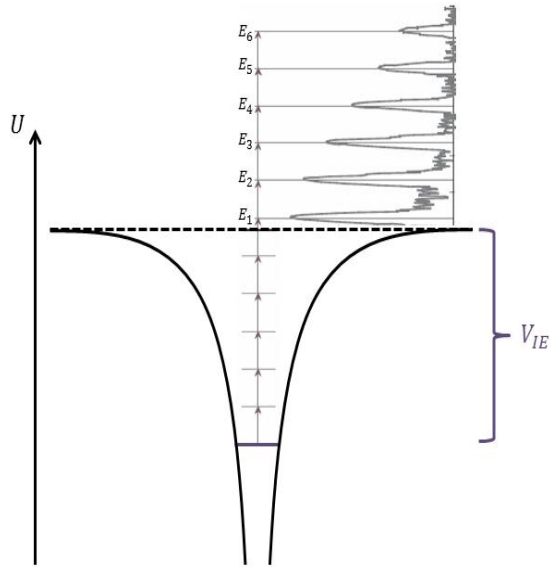

Fig. 7. A graphical depiction of the ATI process. Here the electron absorbs an integer number of photons whose total energy exceeds V_{IE} by more than one photon. The figure shows the graph of a numerical simulation from Paulus, Nicklich, Zacher, Lambropoulos, & Walther (1996) superimposed on to a drawing of an atomic potential well.

If the intensity of the radiation is large, such that the energy of the electron is:

$$E = n\hbar\omega - (V_{IE} + U_P) \tag{2.28}$$

$$< 0 \tag{2.29}$$

the electron will not escape the atom and thus will not appear in the ATI spectrum. As intensity increases, the AC Stark shift (2.13) may exceed the energy of the lower energy peaks successively (see Fig. 8). In such a case, channel closing is said to have occurred and the respective peaks appear suppressed.

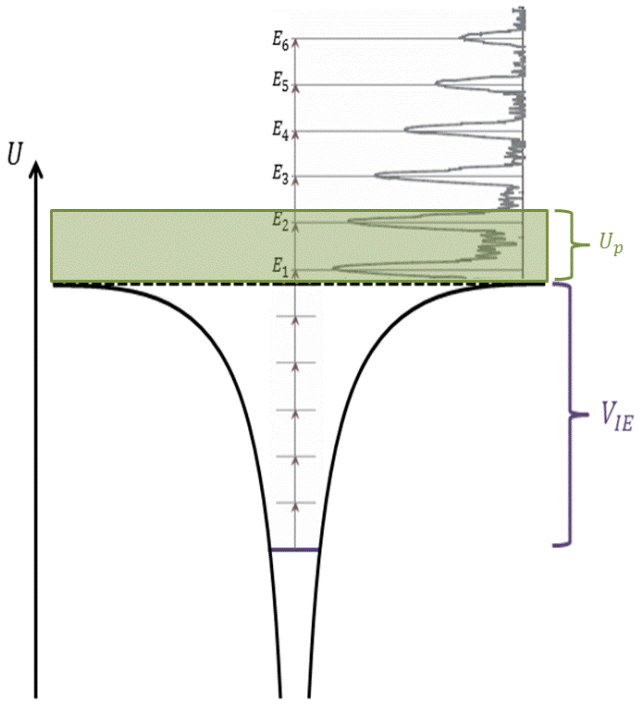

Fig. 8. Channel closing for the E_1 and E_2 peaks of a simulated ATI spectrum.

For sufficiently short pulses low energy electrons will still appear in the ATI spectrum due to a redshifting of the entire spectrum when the electron does not have enough time in the field to regain the ponderomotive energy.

3. SCHEME FOR REALIZATION OF INTENSITY-RESOLVED IONIZATION RATES

A. Basic Principle

The experiment involves ionizing a target gas (xenon) with short pulsed radiation. A series of ATI measurements with xenon are taken at low gas pressure ($< 10^{-5}$mbar) with each measurement having different laser peak intensities. All other laser parameters such as mode quality, pulse duration and spectral bandwidth are kept constant.

B. Experimental Setup

The discussion of this subsection references experimental equipment shown in Fig. 9.The laser oscillator provides 20fs modelocked laser pulses at repetition rate of 80MHz. These pulses were seeded into the laser amplifier which outputs 50fs laser pulses at a repetition of 1kHz. The temporal compression is such that the pulse duration closely matches the transform limited laser pulse. Temporal compression was achieved by maximizing the measured ionization rate within the ATI apparatus using the grating compressor in the laser amplifier. The maximum pulse energy is approximately 0.8mJ.

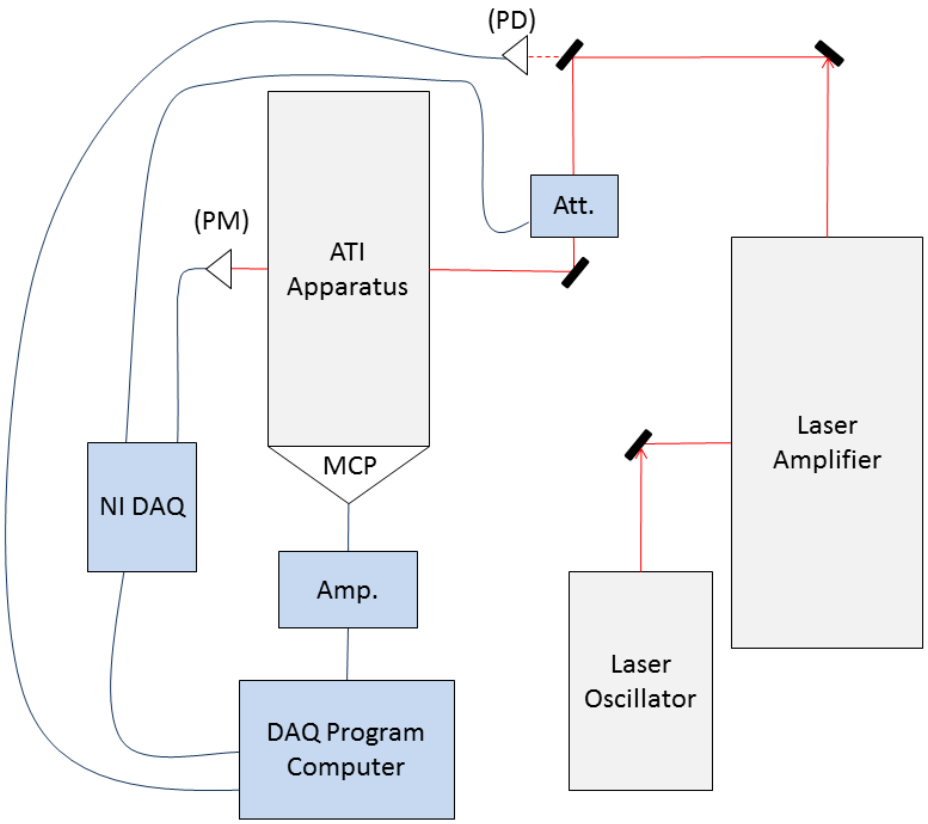

Fig. 9. The experimental setup.

The laser pulses are detected by a photodiode (PD) to trigger the data acquisition software before entering the attenuator (Att.). The radiation is attenuated using a combined half-wave plate and polarizing cube setup. The half wave plate changes the ellipticity of the initially horizontally polarized light, and the polarizing cube filters vertically polarized light out of the laser beam, while horizontally polarized light passes through. The orientation of the wave plate is chosen such that the desired intensity is achieved after the polarizing cube and more importantly at the laser focus.

The laser beam is focused by a lens into ATI apparatus where the target gas is of some known pressure. Ionized electrons are pushed down the TOF tube by the radiation's electric field to the detector or micro-channel plate (MCP) where their TOF

from the laser focus to the detector is recorded. A power meter (PM) measures the average power, determining the average intensity of the radiation, as it leaves the ATI apparatus. This data is first processed to produce intensity vs. ion yield rate (yield of electrons per pulse) curves. This is achieved by dividing the total electron yield for a specific intensity by the number of laser pulses used at this intensity. The data is further processed, using the deconvolution algorithm, to produce intensity vs. ion probability curves.

C. Experimental Equipment

The external features of the ATI setup are pictured in Fig. 10 while the internal features are shown in Fig. 11. It consists of a + shaped vacuum chamber with a Pfeiffer Vacuum (TMU 521) turbo molecular pump and Leybold Vacuum IONIVAC (ITR 200 S) ion gauge to maintain and monitor the vacuum pressure respectively.

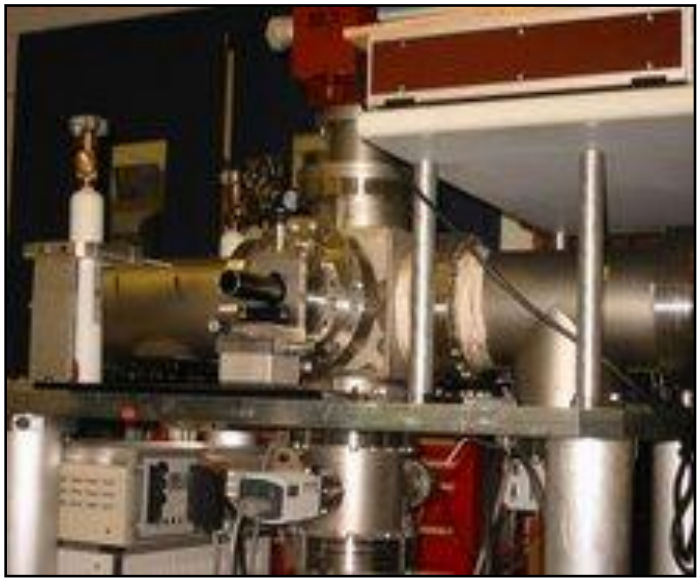

Fig. 10. A photograph taken of the ATI apparatus and related components.

A Leybold Heraeus variable leak valve allows the introduction of the gas (xenon) at desired pressure for a given vacuum pumping rate. The laser beam is first detected, for count triggering purposes, by a fast avalanche photodetector (PD) through the back end of one of the steering mirrors. It is then attenuated to the desired intensity by an 800nm half-wave plate and polarizing cube combination. The laser radiation is focused by a 20cm focal length, 800nm central wavelength, achromatic lens and introduced into the vacuum chamber through a CVI Melles Griot (W2-PW1-2012-UV-670-1064-0) laser quality window. A thermopile, Ophir Nova II power meter was used to measure the average power of the pulse train at the exit window of the ATI apparatus. A set of laser powers determined the values of the intensities used for measurements. A μ-metal drift tube encased the flight path of the ionized electrons as they were detected at the Del Mar Photonics (MCP-MA34/2) microchannel plate.

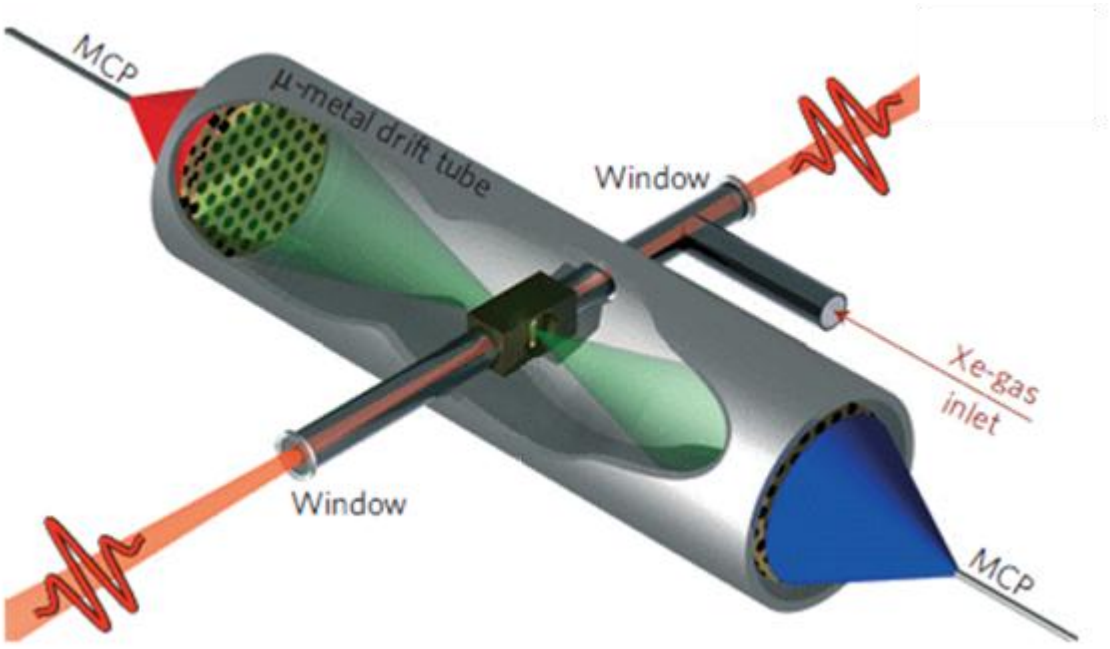

Fig. 11. The essential components of the ATI apparatus.

The signals from the MCP are amplified by a Stanford Research Systems (SR445A) amplifier. The signals from the fast PD and SR445A are digitized by a FAST ComTec (P7887) Multiscaler PCI counting card through its start and stop terminals respectively. A specialized National Instruments LabVIEW 8.5 program is used in conjunction with commercial P7887 data acquisition software from FAST ComTec to record all pertinent data for the experiment.

4. CONVERTING FROM TOF TO ENERGY SPECTRA

A. The Format of Recorded Data

The energy spectra of ionized electrons provides an important and versatile measure of ionization parameters during the experiment. The spacing between the most prominent ATI peaks indicates the average photon energy of the ionizing radiation (Agostini, Fabre, Mainfray, & Petite, 1979). The width of the peaks is a measure of the pulse duration of the radiation. The background envelope of the ATI spectra contains intensity information for many-cycle laser radiation (Paulus, Becker, Nicklich, & Walther, 1994) and phase information for few cycle pulses (Paulus, Grasbon, Walther, Kopold, & Becker, 2001). The sub-peak structure displays the dynamic position of the atomic/molecular energy levels (Lambropoulos, 1993).

The software for the counting card formats the measured data into time of flight (TOF) spectra. The TOF spectra is then converted into an energy spectra using a time bin resorting algorithm. To illustrate this let the TOF spectra be represented by a histogram S_t of electron arrival times t_b. The histogram S_t has $N_t = 10112$ equally spaced time bins of 0.25ns duration. Therefore S_t has units of $(electron\ counts)/(0.25\text{ns})$. In theory, the array t_b records the amount of time it takes for an electron to travel from the ionization region (laser focus) to the detector. In practice it measures the difference in time between the laser trigger and electron detector signals. Each bin $S_{t,i}$ contains the number of electrons that arrive within the $t_{b,i}$ time bin window (see Fig. 12).

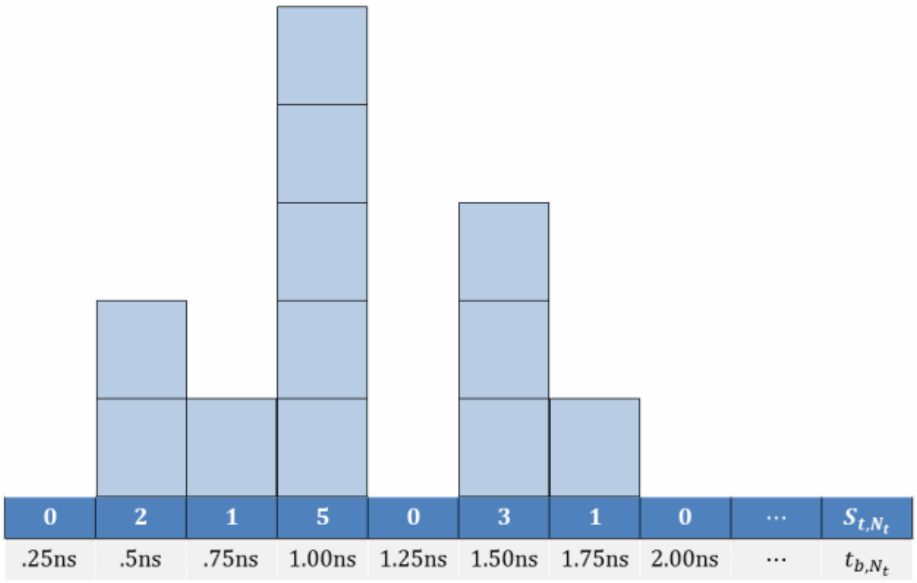

Fig. 12. A visual representation of the time bins $t_{b,i}$ and their electron counts $S_{t,i}$. The schematic starts (left) with $t_{b,1} = 0.25\text{ns}$ and $S_{t,1} = 0$.

The kinetic energy of an electron is denoted:

$$E_i = \frac{m_e {v_i}^2}{2}$$

$$= \frac{m_e}{2}\left(\frac{L}{t_{b,i} + \delta t}\right)^2 \tag{4.1}$$

where m_e is the mass of the electron, L is the distance from the laser focus to the MCP, and δt is timing delay. Both L and δt are free parameters that are adjusted so that known physical properties of an ATI energy spectra are adequately represented. δt is set such that the peaks of the energy spectra are equally spaced by a value ΔE, and L is set such that the spacing ΔE is equal to the central frequency of the laser $\hbar\omega_0 = 1.55\text{eV}$. For the experiment $L = 0.46\text{m}$ and $\delta t = -4.1\text{ns}$.

B. Discrete Conversion to Energy Spectra

In discrete binning, an empty histogram of electron counts in the energy domain is created and denoted by S_E. The energy bins in S_E, denoted $S_{E,j}$, are equally spaced and span the set of energies available to the electrons of interest. The total number of electrons $\sum S_{t,i}$ arriving between times:

$$L\sqrt{\frac{m_e}{2E_{b,j+1}}} < t_{b,i} < L\sqrt{\frac{m_e}{2E_{b,j}}} \tag{4.2}$$

is assigned to an energy bin E_{bj}. This is done successively until all the electrons in S_t have been assigned to energy bins in S_E.

C. Continuous Conversion to Energy Spectra

In continuous binning, the following equation must be satisfied:

$$\int_0^\infty S_t(t)dt = \int_0^\infty S_E(E)dE \tag{4.3}$$

where S_t is the TOF spectra, S_E is the ATI energy spectra. Note that,

$$t = L\sqrt{\frac{m}{2E}} \tag{4.4}$$

and

$$dt = \frac{dt}{dE}dE. \tag{4.5}$$

Plugging equations (4.4) and (4.5) into the right hand side of equation 1 we get:

$$\int_\infty^0 S_t\left(L\sqrt{\frac{m_e}{2E}}\right)\frac{dt}{dE}dE = \int_0^\infty S_E(E)dE \tag{4.6}$$

Comparing equations (4.6) and (4.3) gives:

$$S_E(E) = -S_t(t)\frac{dt}{dE} \tag{4.7}$$

and

$$dE = \frac{dE}{dt}dt \tag{4.8}$$

The expression (4.3) is the time/energy integrated yield of electrons $Y(I)$ measured for some peak laser intensity I. It is useful to calculate $Y(I)$ since it can be used to derive the deconvolution algorithm. The details of this property are discussed in Section 6.

5. GAUSSIAN BEAM GEOMETRY

A Gaussian beam has a spatial profile that is radially symmetric in cylindrical coordinates. The electric field amplitude and intensity as a function of the radial and longitudinal variables r and z respectively:

$$\mathcal{E}(r,z) = \mathcal{E}_0 \left(\frac{w_0}{w(z)}\right) e^{-\frac{r^2}{w^2(z)}} \tag{5.1}$$

$$I(r,z) = I_0 \left(\frac{w_0}{w(z)}\right)^2 e^{-\frac{2r^2}{w^2(z)}} \tag{5.2}$$

where ω_0 is the beam waist, $w(z) = w_0\sqrt{1+\left(\frac{z}{z_R}\right)^2}$ and $z_R = \frac{\pi w_0^2}{\lambda}$. This is referred to as the fundamental transverse mode or TEM_{00} mode of a laser beam. Solving for r^2 we get:

$$r(I,I_0,z)^2 = w^2(z)\ln\left[\frac{I_0}{I}\frac{w_0^2}{w^2(z)}\right] \tag{5.3}$$

The radius $r = 0$ when the argument $\frac{I_0}{I}\frac{w_0^2}{w^2(z)} = 1$, or $z_\pm \equiv \pm z_R\left(\frac{I_0}{I}-1\right)$. Using equation (5.3), the three-dimensional volume of a laser beam with peak intensity I_0 bounded by an intensity I is:

$$V_3(I,I_0) = \pi\int_{z_-}^{z_+} r^2(I,I_0,z)dz \tag{5.4}$$

$$= \pi z_R w_0^2\left\{\frac{4}{3}\left[\frac{I_0}{I}-1\right]^{\frac{1}{2}} + \frac{2}{9}\left[\frac{I_0}{I}-1\right]^{\frac{3}{2}} - \frac{4}{3}\arctan\left[\frac{I_0}{I}-1\right]^{\frac{1}{2}}\right\} \tag{5.5}$$

For two dimensions a cross-sectional slice of the laser gives a disk like volume bounded by an intensity I.

$$V_2(I,I_0) = \pi\, r^2(I,I_0,z)\Delta z \tag{5.6}$$

The one dimensional differential volume is merely a rod along the y axis intersecting the x and z axis of the laser.

$$V_1(I, I_0) = 2r(I, I_0, z)\,\Delta x\,\Delta z \tag{5.7}$$

The space between radii $r(I_i, I_0, z)$ and $r(I_{i+1}, I_0, z)$ for some intensities $I_{i+1} < I_i < I_0$ define an iso-intensity shell confined by I_i and I_{i+1}(see Fig. 13).

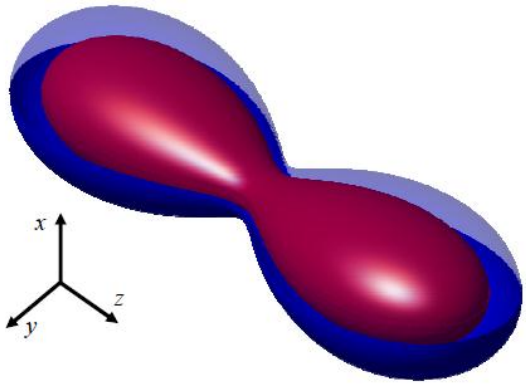

Fig. 13. A depiction of the three-dimensional iso-intensity shells. The blue shell is made transparent in its upper half to reveal an inner red shell of higher intensity. The figure is from Strohaber (2008).

6. REMOVING INTENSITY INTEGRATION

A. Intensity Difference Scanning

In intensity difference scanning an experiment is taken N times, each with a unique peak pulse intensity I_i (usually the average) chosen to represent the intensities of the pulses used for that run. The intensities represent an ordered set $I_i \in \{I_1, I_2, \cdots, I_N\}$ such that $I_1 > I_2 > \cdots > I_N$. One method of resolving the volume independent probability is to divide the volumes into discrete segments. To do this, we define three quantities:

$V_{i,j} \equiv differential\ volume\ element\ for\ intensity\ I_j\ at\ laser\ peak\ intensity\ I_i$

$Y(I_i) \equiv volume\ integrated\ electron\ yield\ rate\ for\ a\ peak\ intensity\ I_i$

$P(I_j) \equiv electron\ yield\ probability\ of\ per\ unit\ volume\ at\ intensity\ I_j,$

which are related by the equation:

$$Y(I_i) \cong \sum_{j=1}^{N} V_{i,j} P(I_j) \tag{6.1}$$

The differential volume elements $V_{i,j}$ can be defined in a number of different ways. However, any definition of $V_{i,j}$ must satisfy:

$$\lim_{N\to\infty} \sum_{j=1}^{N} V_{i,j} P(I_j) = -\int_0^{I_i} P(I) \frac{\partial V(I, I_i)}{\partial I} dI$$

where $\lim_{N\to\infty} |I_j - I_{j+1}| = 0$. For example, $V_{i,j}$ can be defined by taking the difference between the volumes enclosed by two consecutive iso-intensity shells:

$$V_{i,j} \equiv \begin{cases} \left|V(I_j, I_i) - V(I_{j+1}, I_i)\right| & for\ i \geq j \\ 0 & for\ i < j \end{cases} \tag{6.2}$$

This definition follows from the discrete first derivative:

$$\frac{\Delta V(I_j, I_i)}{\Delta I}\Delta I = \left|\frac{V(I_j, I_i) - V(I_{j+1}, I_i)}{I_j - I_{j+1}}\right| \left|I_j - I_{j+1}\right|$$

Since I_N is the smallest element in the list of measured intensities, a free parameter $I_{N+1} \equiv \delta I$ is chosen for the calculation of $V(I_{N+1}, I_i)$ for all i (see Fig. 14). The determination of δI is discussed later at the end of this subsection.

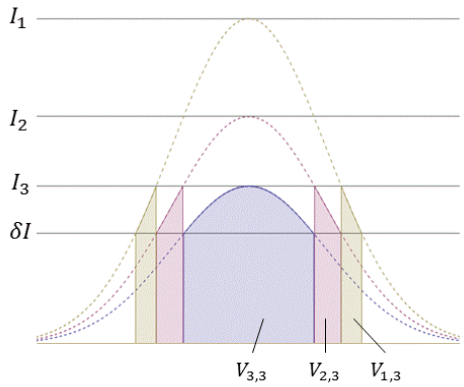

Fig. 14. An example schematic in one dimension showing how volume elements are related to peak intensities. Here the number of experiments $N = 3$. The boundary of each volume (horizontal) is set above and below by intensities δI and I_3 respectively. δI is an arbitrary parameter that provides an outer boundary for the calculation of the volume elements.

If i and j have the same dimensions ($i, j \in \{1,2, \dots, N\}$), (6.1) produces a system of linear equations that can be solved for the desired variable $P(I_j)$.

For example, if we perform an experiment twice ($N = 2$) using different laser peak intensities, $I_1 > I_2$, in one dimension the volume elements are $V_{1,1}$, $V_{1,2}$ and $V_{2,2}$ (see Fig. 15). There is a spatial region unaccounted for in the distribution of intensities with values lower than I_2 that is in principle infinite in size since Gaussian distributions

are never equal to zero. Typically, we assume that the probability, $P(I)$, of measuring ions from the lowest intensities $I < \delta I$ is so small that the outermost volume can be neglected.

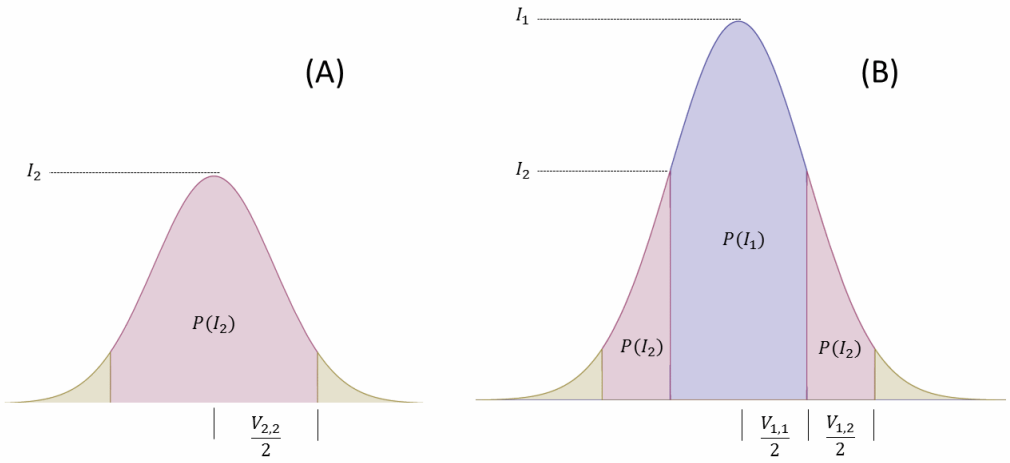

Fig. 15. A scheme showing the relationship between the volume elements ($V_{1,1}$, $V_{1,2}$, $V_{2,2}$) and their respective probabilities ($P(I_1)$, $P(I_2)$, $P(I_2)$). Beam (A) is represented by (6.3) and beam (B) is represented by (6.4).

Using (6.1), the measured ion yield rates for beams (A) and (B) respectively are then approximated by:

$$Y(I_2) = V_{2,2}P(I_2) \tag{6.3}$$

$$Y(I_1) = V_{1,2}P(I_2) + V_{1,1}P(I_1) \tag{6.4}$$

Since the quantities $Y(I_1)$, $Y(I_2)$, $V_{1,1}$, $V_{1,2}$ and $V_{2,2}$ are all known, it is purely a mathematical exercise to solve (6.3) and (6.4) for $P(I_2)$ and $P(I_1)$.

$$P(I_2) = \frac{Y(I_2)}{V_{2,2}}$$

$$P(I_1) = \frac{1}{V_{1,1}}\left(Y(I_1) - \frac{V_{1,2}}{V_{2,2}}Y(I_2)\right)$$

A physical picture of this solution for $V_{1,1}P(I_1)$ is displayed in Fig. 16.

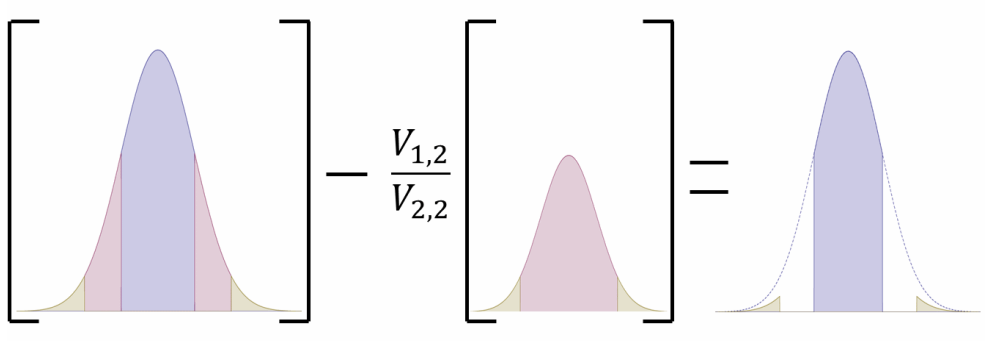

Fig. 16. Graphical depiction of the IDS algorithm using two intensities.

For the general case of N different laser peak intensities we can use (6.1) to calculate a vector $\boldsymbol{Y} \equiv \big(Y(I_1), Y(I_2), \dots, Y(I_N)\big)^T$ and get a system of linear equations:

$$V_{1,1}\,P(I_1) + V_{1,2}\,P(I_2) + \cdots + V_{1,N}\,P(I_N) = Y(I_1)$$

$$V_{2,2}\,P(I_2) + \cdots + V_{2,N}\,P(I_N) = Y(I_2)$$

$$\vdots$$

$$V_{N,N}\,P(I_N) = Y(I_N)$$

This set of linear equations can be conveniently expressed in matrix form:

$$\begin{pmatrix} V_{1,1} & V_{1,2} & \cdots & V_{1,N} \\ 0 & V_{2,2} & \cdots & V_{2,N} \\ \vdots & \vdots & \ddots & \vdots \\ 0 & 0 & \cdots & V_{N,N} \end{pmatrix} \begin{pmatrix} P(I_1) \\ P(I_2) \\ \vdots \\ P(I_N) \end{pmatrix} = \begin{pmatrix} Y(I_1) \\ Y(I_2) \\ \vdots \\ Y(I_N) \end{pmatrix} \tag{6.5}$$

or $\hat{V} \cdot \boldsymbol{P} = \boldsymbol{Y}$. To find $\boldsymbol{P}$ multiply both sides by the inverse volume matrix $\hat{V}^{-1}$ to obtain:

$$\boldsymbol{P} = \hat{V}^{-1} \cdot \boldsymbol{Y} \tag{6.6}$$

A conceptual diagram of this relationship is displayed in Fig. 17.

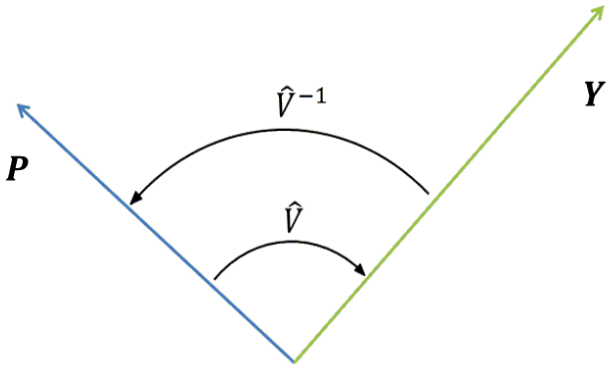

Fig. 17. $\hat{V}$ and $\hat{V}^{-1}$ portrayed as $N \times N$ matrix transformations between $\boldsymbol{Y}$ and $\boldsymbol{P}$.

The free parameter δI represents a problem for the definition (6.2) because its determination requires some knowledge of the probability $P(I_N)$. δI is by definition the intensity I_{N+1} such that $V_{N,N} = Y(I_N)/P(I_N)$. For some simple atoms in the multiphoton regime, the probability $P(I_N)$ can be determined theoretically using perturbation theory (Boyd, 2008).

However, a novel definition of $V_{i,j}$, and more importantly $V_{i,j}^{-1}$, is present in this thesis which does not require the parameter δI.

B. Analytical Volume Deconvolution in M Dimensions

To find the probability for ionizing from a non-integrated laser intensity I present the solution found in (Strohaber, Kolomenskii, & Schuessler, 2010). This solution can be applied to volume deconvolution problems of one, two and three dimensions. For Gaussian beams:

$$Y(I_0) \equiv \int_0^{I_0} P(I) \frac{\partial V(I, I_0)}{\partial I} dI \tag{6.7}$$

$$= \int_0^{I_0} P(I) K\left(I/I_0\right) \frac{dI}{I_0} \tag{6.8}$$

where $P(I)$ is the ionization probability per unit volume and $K(I/I_0) = I_0|\partial V(I, I_0)/\partial I|$. Expanding $Y(I)$ and $P(I)$ into polynomial series we get:

$$Y(I) = {I_0}^m \sum_k A_k \, {I_0}^k \tag{6.9}$$

$$P(I) = I^m \sum_k B_k \, I^k \tag{6.10}$$

The coefficients $A_k$are known through a polynomial fit of the data. The goal now is to obtain the unknown coefficients B_k so that the function $P(I)$ may be calculated. Plugging equation (6.10) into (6.8) gives:

$$\begin{aligned} Y(I_0) &= \int_0^{I_0} \sum_k B_k \, I^{m+k} \, K\left(I/I_0\right) \frac{dI}{I_0} \\ &= \sum_k B_k \, {I_0}^{m+k} \int_0^{I_0} \left(\frac{I}{I_0}\right)^{m+k} K\left(I/I_0\right) \frac{dI}{I_0} \\ &= {I_0}^m \sum_k B_k \, {I_0}^k \int_0^1 \xi^{m+k} K(\xi) d\xi \\ &= {I_0}^m \sum_k \frac{B_k}{G_k} \, {I_0}^k \\ &= {I_0}^m \sum_k A_k \, {I_0}^k \end{aligned}$$

where $G_k^{-1} \equiv \int_0^{I_0} \xi^{m+k} K(\xi) d\xi$. Therefore, by inspection the probability coefficients are:

$$B_k = G_k A_k \tag{6.11}$$

The probability is then calculated from (6.10) as an analytical function.

C. Implementation of the Volume Deconvolution

For analysis purposes it is useful to recast (6.9) into a matrix form. Note that for a discrete set of data points $\boldsymbol{Y}$, (6.9) can be rewritten as:

$$\begin{pmatrix} I_1^m & I_1^{m+1} & \cdots & I_1^{m+n} \\ I_2^m & I_2^{m+1} & \cdots & I_2^{m+n} \\ \vdots & \vdots & \vdots & \vdots \\ I_N^m & I_N^{m+1} & \cdots & I_N^{m+n} \end{pmatrix} \begin{pmatrix} A_1 \\ A_2 \\ \vdots \\ A_n \end{pmatrix} = \begin{pmatrix} Y(I_1) \\ Y(I_2) \\ \vdots \\ Y(I_N) \end{pmatrix} \tag{6.12}$$

or in a more compact form as $\hat{I}_0 \cdot \boldsymbol{A} = \boldsymbol{Y}$. As before, finding the coefficients B_k gives the probability $P(I)$, but first we must find the coefficients A_k. If (6.9) is constructed through an ordinary least squares fit of the data $\boldsymbol{Y}$, then:

$$\boldsymbol{A} = \left(\hat{I}_0^T \hat{I}_0\right)^{-1} \hat{I}_0^T \boldsymbol{Y} \tag{6.13}$$

Using the Strohaber et al. (2010) solution we define a square, diagonal matrix $\hat{G}$ such that:

$$\hat{G} \equiv \begin{pmatrix} G_1 & 0 & \cdots & 0 \\ 0 & G_2 & \cdots & 0 \\ \vdots & \vdots & \ddots & \vdots \\ 0 & 0 & \cdots & G_n \end{pmatrix} \tag{6.14}$$

This gives the $\boldsymbol{B}$ vector:

$$\boldsymbol{B} = \hat{G} \cdot \boldsymbol{A} \tag{6.15}$$

and the probability:

$$\boldsymbol{P} = \hat{I}_0 \cdot \boldsymbol{B} \tag{6.16}$$

$$= \hat{I}_0 \cdot \hat{G} \cdot \boldsymbol{A} \tag{6.17}$$

$$= \hat{I}_0 \cdot \hat{G} \cdot \left(\hat{I}_0^T \hat{I}_0\right)^{-1} \hat{I}_0^T \boldsymbol{Y} \tag{6.18}$$

$$= \hat{V}^{-1} \boldsymbol{Y} \tag{6.19}$$

where $\hat{V}^{-1} = \hat{I}_0 \cdot \hat{G} \cdot \left(\hat{I}_0^T \hat{I}_0\right)^{-1} \hat{I}_0^T$ is the inverse volume matrix.

At this point we must note the importance and universality of the matrix approach. $\hat{V}^{-1}$ is independent of the data itself and, as such, characterizes the algorithm. In fact, $\hat{V}^{-1}$ will characterize any algorithm that transforms $\boldsymbol{Y}$ to $\boldsymbol{P}$, given that such a matrix exist.

D. Error Propagation Through the Algorithm

Typically, in an experiment there exists statistical error which interferes with the interpretation of a measurement. The yield rate measured $\boldsymbol{Y}$, in a well-constructed experiment, is approximately but not necessarily equal to its expectation value $\overline{\boldsymbol{Y}}$. These errors diminish the precision of the data and interfere with any attempt to recover the probability vector $\overline{\boldsymbol{P}}$. Instead we recover a probability vector $\boldsymbol{P} = \overline{\boldsymbol{P}} + \Delta\boldsymbol{P}$ where $\Delta\boldsymbol{P}$ is the error in the probability.

Since $\boldsymbol{Y}$ represents the rates of signals arriving at the detector, the statistical error in $\boldsymbol{Y}$ can be modeled by a Poisson distribution. With this distribution the variance is well known to be equal to its average value ($\approx \bar{Y}_i$). Therefore the variance of $Y_i \equiv Y(I_i)$ is:

$$\sigma_{Yi}{}^2 \equiv (Y_i - \bar{Y}_i)^2 \tag{6.20}$$

$$= \bar{Y}_i \tag{6.21}$$

for each element in $\boldsymbol{Y}$.

The variance of $P_i \equiv P(I_i)$ can be found from the definition of its variance:

$$\sigma_{Pj}{}^2 \equiv \left(P_j - \bar{P}_j\right)^2 \tag{6.22}$$

Now to find P_j and $\bar{P}_j$ note that (6.6) gives $\boldsymbol{P} = \hat{V}^{-1} \cdot \boldsymbol{Y}$ and $\overline{\boldsymbol{P}} = \hat{V}^{-1} \cdot \overline{\boldsymbol{Y}}$. Plugging these relations into (6.22) gives:

$$
\begin{aligned}
{\sigma_{Pj}}^2 &= \left(\sum_{i=1}^{N} V_{ji}^{-1} Y_i - \sum_{i=1}^{N} V_{ji}^{-1} \bar{Y}_i\right)^2 \\
&= \left(\sum_{i=1}^{N} V_{ji}^{-1} (Y_i - \bar{Y}_i)\right)^2 \\
&= \left(\sum_{i=1}^{N} \left(V_{ji}^{-1}\right)^2 (Y_i - \bar{Y}_i)^2\right) \\
&\qquad + \left(\sum_{i=1}^{N}\sum_{l=1}^{N} V_{ji}^{-1} V_{jl}^{-1} (Y_i - \bar{Y}_i)(Y_l - \bar{Y}_l)\right. \\
&\qquad \left. - \left(\sum_{i=1}^{N} \left(V_{ji}^{-1}\right)^2 (Y_i - \bar{Y}_i)^2\right)\right) \\
&= \sum_{i=1}^{N} \left(V_{ji}^{-1}\right)^2 \sigma_{Yi}^2 \\
&\qquad + \sum_{i,l:i\neq l} V_{ji}^{-1} V_{jl}^{-1} (Y_i - \bar{Y}_i)(Y_l - \bar{Y}_l)
\end{aligned}
\tag{6.23}
$$

where the first and second terms in (6.23) are the variance and covariance of $\boldsymbol{Y}$ projected on to $\boldsymbol{P}$. Since statistical errors in $\boldsymbol{Y}$ are not correlated the expectation value of the covariant term vanishes. From here, the standard deviation of the probability is calculated.

$$
\sigma_{Pj} = \sqrt{\sum_{i=1}^{N} (V_{ji}^{-1})^2 \sigma_{Yi}^2} \tag{6.24}
$$

E. Runge's Phenomenon

The algorithm (6.19) requires a finite polynomial expansion of order $n \leq N$. When $n = N$ the intensities I_i are known as the nodes of an interpolating polynomial. It is well known in the field of numerical analysis that the spacing of the nodes I_i affects the stability of the polynomial fit, and thus, the algorithm. For the case of equally spaced nodes ($I_{i-1} - I_i = I_i - I_{i+1}, \forall i$), Carl Runge (Runge, 1901) noticed that an oscillatory divergence occurs between the interpolating polynomial and the original generating function. More specifically the interpolating function tends to oscillate erroneously with increasing amplitude toward the boundaries of the interpolation interval (see Fig. 18).

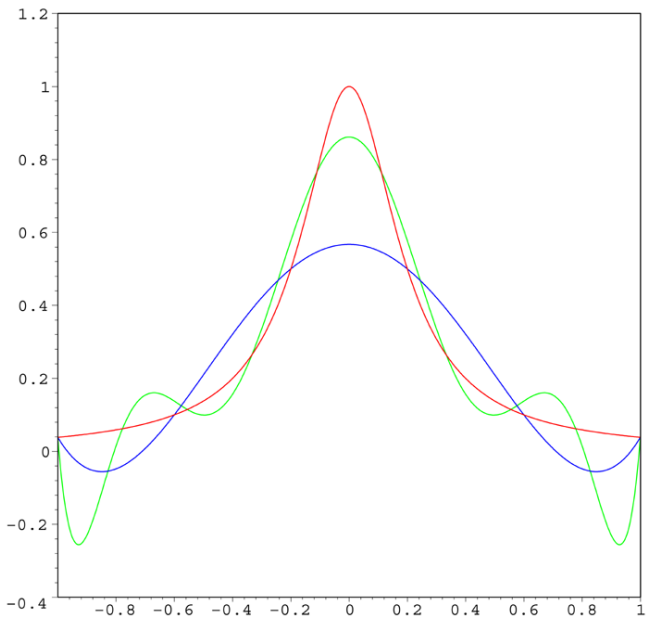

Fig. 18. Interpolating polynomials of degree 5 (blue) and 9 (green) and their generation function (red). The figure is from Runge's Phenomenon (2011).

The problem, known as Runge's Phenomenon, is only made worse when increasing the polynomial order n. This is analogous to what would be expected with the Gibbs Phenomenon in Fourier analysis.

However, the effect of Runge's Phenomenon is mitigated by using nodes that are more densely spaced at the boundaries of the interpolated interval. A specific node spacing called Chebyshev nodes minimizes the divergence between the original generating function and the interpolating polynomial. For an intensity range $I_N < I < I_1$, the Chebyshev nodes are:

$$I_i = \frac{1}{2}\left((I_N + I_1) + (I_N - I_1)\cos\left[\pi\frac{2i-1}{2N}\right]\right) \tag{6.25}$$

Once these nodes are determined, the yield rate $Y(I_i)$ is measured experimentally for each I_i and the $\boldsymbol{A}$ vector is calculated from (6.13). The Runge divergence can be calculated by taking the difference between the original probability function and the interpolating polynomial:

$$P(I) - f_N(I) \leq \frac{P^{(N+1)}(\xi)}{(N+1)!}\prod_{i=1}^{N}\left(\frac{I - I_i}{I_1 - I_N}\right) \tag{6.26}$$

where ξ maximizes $P^{(N+1)}(\xi)$ on the interval $I_N \leq \xi \leq I_1$. Note that (6.26) requires $P(I)$ be differentiable at ξ up to order $N+1$. This obviously cannot be done discretely on the data set, itself only containing N values. So a mock function which closely reproduces the expectation value of the data should be used for $P(I)$.

7. ANALYSIS OF EXPERIMENTAL DATA

In the following, experimental data of xenon ATI are presented with a discussion concerning the reliability of the intensity-resolved ionization probability. The experiment involved the ionization of xenon ($V_{IE} = 12.15\text{eV}$) using horizontally polarized 800nm, 50fs radiation and peak intensities ranging from 4.5×10^{13} to $7.4 \times 10^{14}\text{W/cm}^2$. The data $\boldsymbol{Y}$ in Fig. 19 represents the yield rate of electrons collected from a three-dimensional focal volume with a Rayleigh range of ~0.4mm.

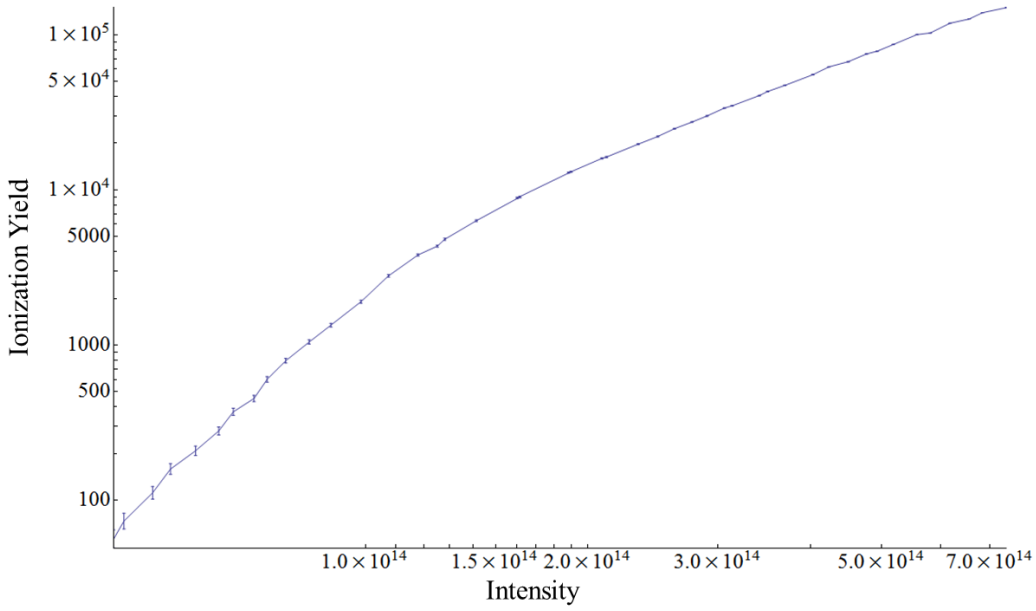

Fig. 19. The photoelectron yield rate for xenon. The data represents a scan of 54 intensities I_i. The error bars represent one standard deviation σ_Y in the yield distribution.

The saturation intensity is calibrated with measured xenon ion yields by Larochelle, Talebpour, & Chin (1998). Since intensities used in the experiment are exponentially spaced according to the formula:

$$I_i = I_{max}\left(\frac{I_{min}}{I_{max}}\right)^{\frac{N-i}{N-1}} \tag{7.1}$$

where I_{min} and I_{max} are the minimum and maximum intensities of the set, Runge's phenomenon dominates the error in the probability at higher intensities. Calculating the Runge divergence requires an analytic generating function, so the model xenon probability:

$$P(I) = \frac{(I/I_S)^{n_o}}{1 + (I/I_S)^{n_o}} \tag{7.2}$$

was use for its calculation where $I_S = 10^{14}\mathrm{W/cm^2}$ is the measured saturation intensity and $n_o = 8$ is the multiphoton order for 1.55eV photons.

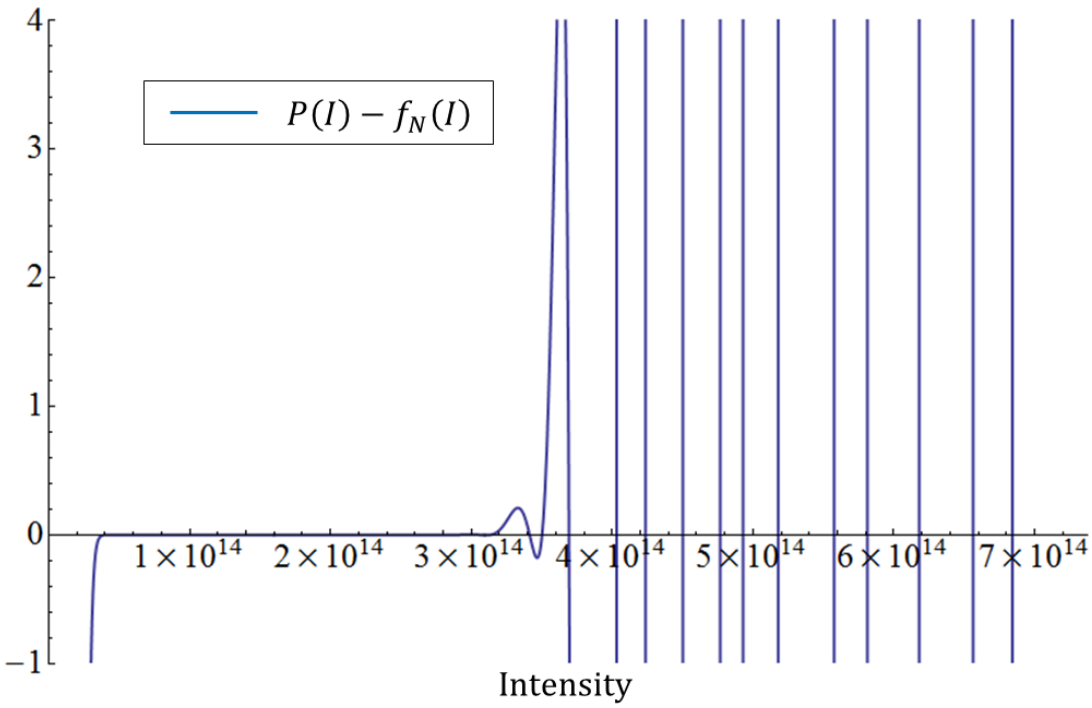

Fig. 20. The Runge divergence calculated for the model xenon probability function $P(I)$ using (6.26). The error is defined to be the difference between the probability and its interpolation function $f_N(I)$. This calculation indicates that probabilities measured at intensities between 5×10^{13} and $3\times10^{14}\mathrm{W/cm^2}$ are virtually free from polynomial interpolation problems.

The results graphed in Fig. 20 show the Runge divergence for the intensity spacing (7.1). The probability $\boldsymbol{P}$ retrieved from the data $\boldsymbol{Y}$ through (6.19) is shown in Fig. 21. The probabilities recorded in the $5 \times 10^{13}\mathrm{W/cm^2} \leq I \leq 3 \times 10^{14}\mathrm{W/cm^2}$ window are not affected by the Runge divergence.

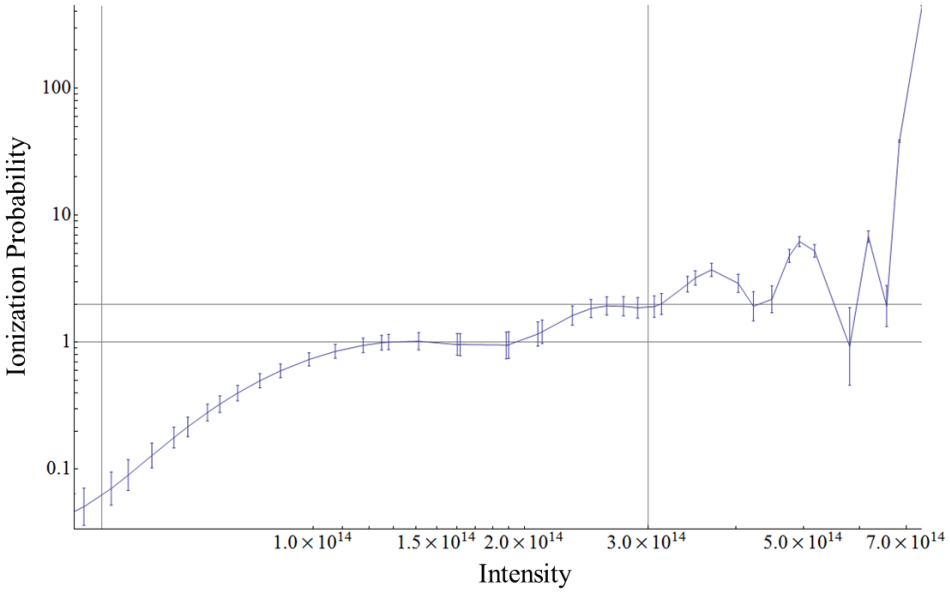

Fig. 21. The intensity-resolved probability of the data. The error bars correspond to the standard deviation σ_Y being propagated through the algorithm. The horizontal lines correspond to ionization probabilities of 1.0 and 2.0. The interpretation of the second line is that the double ionization has occurred. The oscillatory divergence at intensities less than $5 \times 10^{13}\mathrm{W/cm^2}$ and greater than $3 \times 10^{14}\mathrm{W/cm^2}$ are attributed to the Runge's phenomenon.

The graph of the probability reaches 2.0 at approximately $2.7 \times 10^{14}\mathrm{W/cm^2}$. This is attributed to double ionization. Both ion species, Xe^{+} and Xe^{+2}, have a unique probability function that approaches unity as intensity increases. However, they have different saturation intensities. The MCP detector cannot distinguish between electrons from different ion species. Therefore, their yields and, by implication, their probabilities are summed giving a "stair step" appearance to Fig. 21.

The counting electronics naturally groups the electrons according to when they arrive or their TOF. By transforming this time-series to an energy spectra (see Section 5 pp.20) and applying (6.19) to the yield rates for each electron energy the intensity-resolved (volume independent) energy spectra are obtained. Two such spectra are plotted below (see Fig. 22 & Fig. 23).

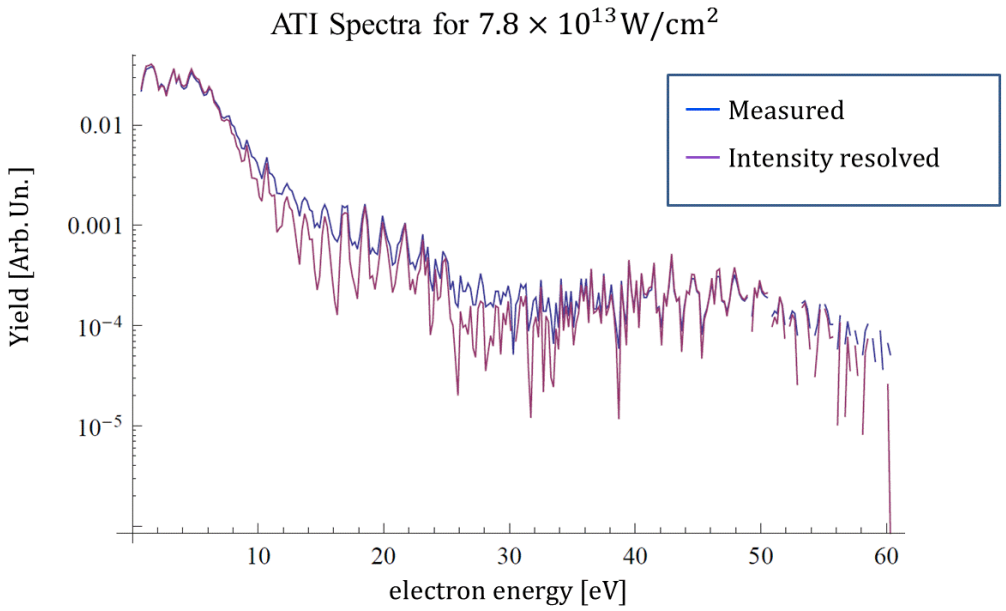

Fig. 22. Intensity-resolved ATI energy spectra at $7.8 \times 10^{13}\mathrm{W/cm^2}$. The blue curve is the measured data prior to being deconvolved.

For the following discussion of features in the ATI spectra see Fig. 23. The first plateau, between 0eV and 8eV, is the result of "direct" electrons that do not scatter off the parent ion after being ionized. These electrons have a classical cutoff energy of $2U_P$ (Paulus, Becker, Nicklich, & Walther, 1994).

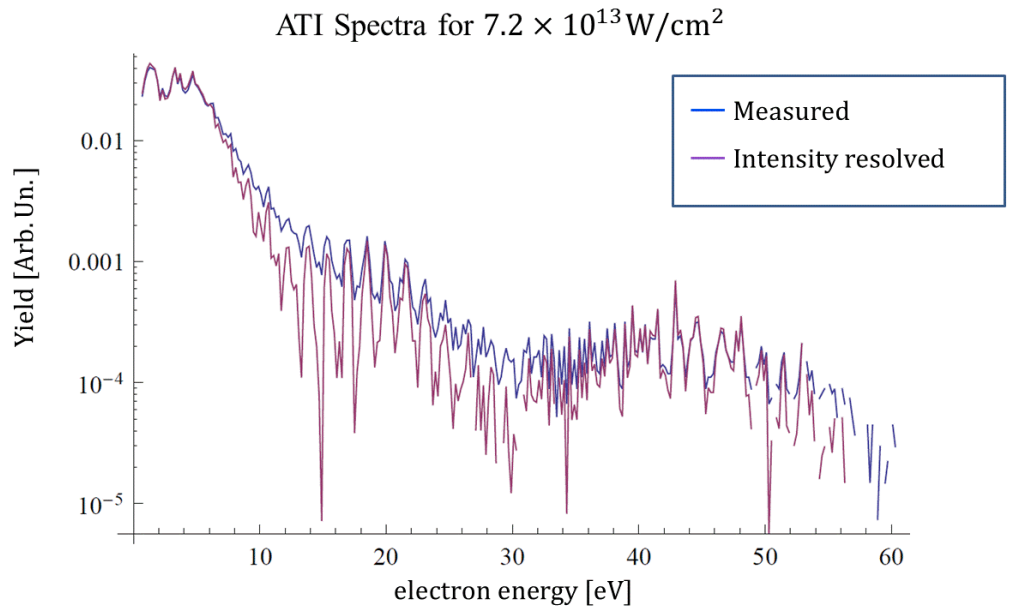

Fig. 23. Intensity-resolved ATI energy spectra at $7.2 \times 10^{13}\mathrm{W/cm^2}$. The blue curve is the measured data prior to being deconvolved.

The second plateau, between 12eV and 25eV, is the result of interference between electrons ionized at different phases of the laser pulse. As electrons are ionized at different electric field maxima, the electrons' phases constructively interfere with each other far away from the focus (Becker, Grasbon, Kopold, Milosevic, Paulus, & Walther, 2002). The effect is more pronounced with longer pulse durations and varies with the atom being ionized. The third plateau, which ranges from 30eV to 45eV, corresponds to elastic backscattering of the electron off the parent ion. This plateau has a cutoff energy of $10.007U_P$ due to the maximum classical energy that a backscattered electron can have (1994). The ponderomotive energy of the laser field exceeds the photon energy. However, because of the short pulse duration the entire energy spectrum is red shifted (see Sections 2.A and 2.E), and we do not see peak suppression due to channel closing in the spectra.

8. SUMMARY AND CONCLUSION

The volume integration of the laser focus reduces the intensity resolution of an experimental measurement. This lack of resolution masks intensity dependent phenomenon such as the AC Stark shifts and Rabi oscillations in the atomic energy levels (Lambropoulos, 1993).

We were able to apply an intensity deconvolution algorithm to the photoelectron yield and obtain intensity-resolved ATI spectra for Xe^+. The algorithm was shown to be robust within a certain range of intensities.

The data suggest that both single and double ionization may be observed in the electron yield. This opens the possibility of obtaining ATI spectra for ions as well as atoms by subtracting the yield of a single ionization with a maximum probability of 1.0. Additionally, intensity-resolved ATI spectra open the possibility of observing with greater detail the effects of Rabi oscillations in alkali atoms, which is the subject of future work.

The error analysis suggests several ways to improve the experiment presented in this thesis. Firstly, the signal to noise ratio in the yield (see Fig. 19) is smallest at lower count rates and correspondingly lower intensities. Therefore, the precision of the experiment may be improved by increasing the target gas (xenon) pressure to increase the count rate. Secondly, the stability of the deconvolution algorithm critically depends on the node (intensity) spacing. Therefore, Chebyshev nodes should be used to improve the accuracy of the algorithm for a larger range of intensities.

REFERENCES

Agostini, P., Fabre, F., Mainfray, G., & Petite, G. (1979). *Phys. Rev. Lett.*, **42**, 1127.

Becker, W., Grasbon, F., Kopold, R., Milosevic, D., Paulus, G., & Walther, H. (2002). *Adv. At. Mol. Opt. Phys.*, **48**, 35.

Boyd, R. W. (2008). "Nonlinear Optics (3rd ed.)." Academic Press, Burlington, MA, US.

Bryan, W. A., Stebbings, S. L., English, E. M., Goodworth, T. R., Newell, W. R., McKenna, J., et al. (2006a). *Phys. Rev. A*, **73**, 013407.

Bryan, W. A., Stebbings, S. L., McKenna, J., English, E. M., Suresh, M., Wood, J., et al. (2006b). *Nature Phys.*, **2**, 379.

Delone, N. B., & Krainov, V. P. (1994). "Multiphoton Processes in Atoms." Springer, Berlin.

Hansch, P., & Van Woerkom, L. D. (1996). *Opt. Lett.*, **21**, 1286.

Keldysh, L. V. (1965). *Sov. Phys. JETP*, **20**, 1307.

Lambropoulos, P. (1993). *AIP Conf. Proc.*, **275**, 499.

Larochelle, S., Talebpour, A., & Chin, S. L. (1998). *J. Phys. B: At. Mol. Opt. Phys.*, **31**, 1201.

Paulus, G. G., Becker, W., Nicklich, W., & Walther, H. (1994). *J. Phys. B*, **27**, L703.

Paulus, G. G., Grasbon, F., Walther, H., Kopold, R., & Becker, W. (2001). *Nature*, **414**, 182.

Paulus, G. G., Nicklich, W., Zacher, F., Lambropoulos, P., & Walther, H. (1996). *J. Phys. B*, **29**, L249.

Runge, C. (1901). *Zeitschrift für Mathematik und Physik*, **46**, 224.

Runge's phenomenon. (2011, April 27). Retrieved June 10, 2011, from Wikipedia: http://en.wikipedia.org/wiki/Runge%27s_phenomenon

Strohaber, J. (2008). Ph.D. Dissertation. University of Nebraska.

Strohaber, J., Kolomenskii, A. A., & Schuessler, H. (2010). *Phys. Rev. A*, **82**, 013403.

Walker, M. A., Van Woerkom, L. D., & Hansch, P. (1998). *Phys. Rev. A*, **57**, R701.

VITA

Name:	Nathan Andrew Hart
Address:	Texas A&M Physics Department, TAMU4242, College Station, TX 77843
Email Address:	n3902@tamu.edu
Education:	B.S., Physics, Texas A&M University, 2006 M.S., Physics, Texas A&M University, 2011